The Role of Feedforward and Feedback Inhibition in Modulating Theta-Gamma Cross-Frequency Interactions

Dimitrios Chalkiadakis[1,2], Jaime Sánchez-Claros[2], Víctor J López-Madrona[3], Santiago Canals[1,*], Claudio R. Mirasso[2,*]

[1]Instituto de Neurociencias, Consejo Superior de Investigaciones Científicas, Universidad Miguel Hernández, Sant Joan d'Alacant, Spain

[2]Instituto de Física Interdisciplinar y Sistemas Complejos (IFISC, UIB-CSIC), Campus UIB, Palma de Mallorca, Spain

[3]Aix Marseille Univ, INSERM, INS, Inst Neurosci Syst, Marseille, France

* Correspondence:

Claudio R. Mirasso

claudio@ifisc.uib-csic.es

Santiago Canals

scanals@umh.es

Abstract

Interactions among oscillatory brain rhythms play a crucial role in organizing neuronal firing sequences during specific cognitive functions. In memory formation, the coupling between the phase of the theta rhythm and the amplitude of gamma oscillations has been extensively studied in the hippocampus. Prevailing perspectives suggest that the phase of the slower oscillation modulates the fast activity. However, recent metrics, such as Cross-Frequency Directionality (CFD), indicate that these electrophysiological interactions can be bidirectional. In this computational study, we demonstrate that the connectivity structure of common neural motifs crucially determines interaction directionality. Specifically, we found

that feedforward inhibition modeled by a theta-modulated ING (Interneuron Network Gamma) mechanism induces fast-to-slow interactions, while feedback inhibition through a PING (Pyramidal Interneuron Network Gamma) model drives slow-to-fast interactions. Importantly, in circuits combining both feedforward and feedback motifs, as commonly found experimentally, directionality is modulated by synaptic strength within realistic ranges, with the feedforward recruitment of inhibitory basket cells playing a critical role in directionality. Finally, we report that each theta-gamma interaction scheme, determined by the balance between feedforward and feedback inhibition, prioritizes distinct modes of information transmission and integration, adding computational flexibility. Our results offer a plausible neurobiological interpretation for cross-frequency directionality measurements associated with the activation of different underlying motifs that serve distinct computational needs.

Author Summary

This study investigates the interaction between various types of brain oscillations and their potential relationship with the connectivity of underlying neural networks. Brain activity encompasses slow oscillations, such as theta, alpha, and delta oscillations, as well as faster oscillations, including gamma oscillations. These oscillations interact through Cross-Frequency Coupling (CFC), a mechanism essential for cognitive processes like memory, learning, and attention. Given the higher spectral power and broader spatial propagation of slow oscillations, it has been proposed that CFC arises when slow oscillations modulate faster activity. However, recent evidence suggests that gamma oscillations can also predict the phase of slower oscillations, indicating a bidirectional and more intricate relationship. To explore this complexity, we developed a computational model that reproduces both forms of interaction observed experimentally. Our results demonstrate that while slow oscillations originating from distant regions can induce gamma activity, local connectivity and specific cell-type dynamics allow gamma oscillations to anticipate slow oscillations in certain conditions. The balance of inhibitory circuits modulates fast-slow oscillation interactions, creating distinct functional modes with varying computational properties and enhancing system flexibility. This work integrates competing hypotheses on oscillation interactions and offers a conceptual framework for linking these dynamics to the structural organization of neural circuits.

Introduction

Mammalian brains exhibit oscillatory activity over a broad frequency range, from 0.5 to 500 Hz, spatially organized across different regions [1]. These oscillations reflect distinct synchronization patterns of the underlying neural circuits and are associated with different behavioral states. For instance, theta band oscillations, around (4-8) Hz, in the prefrontal cortex and hippocampus and alpha band oscillations, around (8-12) Hz, in the visual cortex, have been linked with locomotion, learning, and attention [2, 3, 4, 5, 6].

Faster rhythms, such as gamma oscillations within the 30-150 Hz frequency band, are also ubiquitous in brain networks [7, 8]. Notably, gamma oscillations frequently interact with slower rhythms in a phenomenon known as cross-frequency coupling (CFC) [9]. The hippocampus in particular, has been extensively studied for its theta-gamma CFC, which shows increased gamma amplitude locking to the phase of the theta cycle during decision-making and learning [10, 11, 12]. Additionally, CFC has been observed in the cortex, where gamma activity couples with theta, alpha, and beta oscillations [13]. Theories of neural computation propose that CFC plays a critical role in inter-regional communication essential for attention [14], and in organizing neuronal firing into cell assembly sequences underlying episodic memory formation [15].

The generation of CFC, though not fully understood, has been explained based on local and global network properties. *In vitro* and computational studies implicated intrinsic neuronal properties, such as I_h currents, and interactions between fast and slow interneurons, as key local mechanisms [16, 17, 18, 19, 20]. Simultaneous electrophysiological recordings in the hippocampus and entorhinal cortex showed, however, that CFC was also influenced by rhythmic inputs from upstream layers [21, 22, 23]. Additionally, the finding of high coherence at low frequencies across distant recording sites, but not at high frequencies, led to the concept that slow oscillations are driven by upstream areas, which then locally organize faster network dynamics [24, 25, 26]. This aligns with the oscillatory hierarchy hypothesis, which posits that slower oscillations modulate population excitability, thereby coordinating higher-frequency activity [27].

However, the application of techniques for separating field potentials into pathway- or layer-specific activity patterns-combined with new metrics that assess directional interactions across frequency bands, such as cross-frequency-directionality (CFD) [28], has revealed bidirectional interactions between fast and slow oscillations. In the hippocampus, recordings from rats engaged in navigation and memory tasks demonstrated that bouts of gamma activity systematically preceded the phase of theta oscillations, suggesting gamma-to-theta interaction [12] (see Fig. 1a).

Similarly, human electrocorticography studies have reported gamma-to-alpha interaction directionality in the visual cortex [28]. Furthermore, using two independent methods to assess directionality, Dupret and colleagues [29] observed both directionalities: theta-to-gamma in the hippocampus during REM sleep in rats, and gamma-to-theta in the human auditory cortex. Overall, CFC is not exclusively due to slow-to-fast interactions challenging the conventional oscillatory hierarchy hypothesis.

In this study, we aim to (1) address and reconcile this discrepancy by employing a computational modeling approach and (2) offer a plausible neurobiological interpretation of CFD. Specifically, we adapt a model from the work of [30] to investigate the underlying mechanisms and provide new insights. In our model, pyramidal neurons receive inputs from an external population generating a slow (theta) rhythm, while the fast (gamma) rhythm emerges locally through the activity of fast-spiking interneurons. We found that the local cross-frequency directionality is determined by the dominance of specific connectivity motifs within the underlying circuit. In a theta-modulated Interneuron Network Gamma (θ-ING) motif (Fig. 1b), feedforward recruitment of fast-responding interneurons primarily drives gamma-to-theta directionality. In contrast, in theta-modulated Pyramidal-Interneuron Network Gamma (θ-PING) motif (Fig. 1c), feedback inhibition supports theta-to-gamma directionality. In combined motifs that reflect the anatomy of neuronal circuits commonly found in the brain, we analyzed transitions between these modes, demonstrating smooth bidirectional interactions controlled by synaptic strength within biologically plausible ranges. Finally, we evaluated each motif's capacity to integrate distinct inputs, uncovering a mechanism to prioritize transmission in parallel information channels in the dendrite of pyramidal cells.

Materials and Methods

Theta-gamma generation in the θ-ING and θ-PING motifs

The two motifs analyzed in this study are variations of the famous Interneurons Network Gamma (ING) and Pyramidal-Interneuron Network Gamma (PING) models which are known to create gamma activity through interactions between pyramical cells (PCs) and fast spiking inhibitory interneurons, mostly parvalbumin-immunoreactive basket cells (BCs) [31, 21, 33, 35]. A gamma cycle starts with BCs firings, that suppresses the spiking of their target neurons, including other BCs. Then, the inhibition decays at a rate governed by the $GABA_A$ receptor decay time, allowing the BCs

to spike again and thereby initiate a new cycle. The excitatory drive—whether constant or stochastic— could originate either from outside of the network (ING) or due to bidirectional connections of the BC with PCs (PING). In the PING mechanism PCs fire at the onset of each cycle exciting the BC, which then inhibit both populations. The cycle restarts when the pyramidal cells overcome the inhibition.

The model exhibits CFC because gamma dynamics are tuned on and off in theta due to an externally imposed excitatory input (Fig. 1b-i, 1c-i). The θ input is modeled such that each cycle is separated from the previous one by an inter-cycle period, T_{cycle}, drawn from a Gaussian distribution with a mean μ_T=125 ms and a standard deviation of σ_T=16 ms. Each cycle contains 10,000 spikes, distributed according to a second Gaussian with a standard deviation of w=25 ms. The variability in both inter- and intra-cycle timing, controlled by σ_T and w, respectively, is essential since the phase slope index metric that we employ here detects interactions between signals in broad frequency bands.

In order to make meaningful comparisons between the two motifs we use the same synaptic weights for shared connections while the PCs→BCs synaptic weight of the θ-PING is chosen so that the mean firing rate of the PCs are almost identical in both motifs. For instance, in Fig. 1 the firing rates are $f_{r,\theta\text{-ING}}$=0.48(0.01) Hz and $f_{r,\theta\text{-PING}}$=0.49(0.01) Hz where the number represents the mean value and the parenthesis denotes the standard deviation across 20 simulations. Nonetheless, the emergent gamma oscillations in the θ-ING and θ-PING motifs differ, with θ-ING motif exhibiting faster dynamics (Fig. 1b-ii,iv vs 1c-ii,iv). This occurs because the θ input's strength was set to a relatively low level, causing sparse firing of the individual neurons at a rate lower than the population frequency, similar to what is observed in vivo. This discrepancy is even more pronounced in the PCs, to the extent that the computational models replicating this behavior fall under the weak PING/ING subcategory [36]. Thus, due to their low input and slower dynamics, PCs collectively need more time to elicit a synchronized activity in the θ-PING case compared to the BCs of the θ-ING model, which are driven directly from the θ input.

Cells

Although the motifs we analyzed are ubiquitous in multiple brain areas, our model was adapted from previous works modeling the hippocampus CA3 area by [30]. Pyramidal cells were represented as multi-compartmental neurons while basket cells were modeled as single-compartment. Both neuron types included leak, transient sodium, and delayed rectifier potassium currents, with PCs also incorporating hyperpolarization-activated currents. For a comprehensive description of the model see also [37] and the simulations code available in GitHub.

Modeling multicompartmental pyramidal cells with dendrites enables the simulation of realistic transmembrane currents and Local Field Potential (LFP) recordings [38]. To that matter, our PCs consist of 5 compartments, each one consisting of 3 segments for higher accuracy in spatial integration. Panels (b-i) and (c-i) of Fig. 1 depict a scheme of the model including the morphology of the PC. From top to bottom, 3 compartments emulate the apical dendrites, one the soma and the final one the basal dendrites. All compartments are modeled as cylinders.

As far as the BCs dendrites are concerned we chose not to model them explicitly following ref. [30]. Nonetheless, since, dendritic transmission time in BCs is small yet not negligible, we included a fixed delay of 1 ms from the external driver to the basket cells. This dendritic delay was chosen so that it is larger than the onset between evoked dendritic postsynaptic currents and the associated increase of the somatic membrane potential in patch clamp experiments (see Fig. 3d of [39]).

Synapses

Our model includes three types of synaptic connections between neurons: inhibitory $GABA_A$, excitatory AMPA, and excitatory NMDA. Unless stated otherwise, synaptic weights for NMDA connections are set to a fixed value ten times lower than those for AMPA. Neuronal connections are random. Axonal propagation and synaptic transmission delays between populations x and y are modelled through the transmission delay $\tau_{x,y}$, drawn from a Gaussian distribution with a standard deviation of 0.2 ms. The mean delays are: $\tau_{\theta,BC}$=20 ms, $\tau_{\theta,PC}$=20 ms, $\tau_{BC,PC}$=1.5 ms, $\tau_{PC,BC}$=1.5 ms, and $\tau_{BC,BC}$=1.5 ms unless otherwise specified. To account for unmodeled sources, poissonian noise sources with a rate of 1 ms and no transmission delay are added to the pyramidal soma, proximal dendrites, and basket cells. In the simulations of Fig. 5, we call the poissonian source at the proximal dendrite as “parallel pathway” since it plays a more significant role, with its synaptic strength increased tenfold and its rate adjusted from 1 ms to 5 ms. Synaptic parameter values are listed in Tables S1 and S2.

Simulations

Simulations were conducted using the NEURON simulator library [40]. Each simulation modeled 60 seconds of activity across 20 realizations, with different instances of the poissonian and θ-inputs. The only exception to this were simulations used to produce Fig. 5 where, depending on the protocol, an specific’s input instance was kept fixed between simulations whereas the rest of the inputs had different instances. Each simulation included 200 PCs and 40 BCs.

Analysis

Cross Frequency Coupling

This metric aims to quantify the degree to which the amplitude of a signal at a given high frequency f_{high} co-modulates with the phase at a different low frequency f_{low}. Various metrics have been developed for this purpose, but we will use the one proposed by [41] also known as the mean vector length. This method involves first filtering the signal at both f_{high} and f_{low}, followed by the calculation of the analytic signal's amplitude at high frequencies $A_{high}(t)$ and the analytic signal's phase at low frequencies $\varphi_{low}(t)$. Next, we construct the composite signal $z(t)=A_{high}(t)\exp(i\varphi_{low}(t))$, which resides in the complex plane. If there is no coupling between the selected frequencies, the trajectory of z(t) will be radially symmetric. Consequently, the absolute average of the composite signal, $|z_{avg}(t)|$, is zero when there is no CFC, while positive otherwise. In this study, we used the Comodulogram class from the pactools Python library created by [29] to extract $|z_{avg}(t)|$.

To statistically assess the significance of the results, we employ a surrogate analysis following [28]. We generate 1,000 surrogate time series by randomly splitting the phase signal into two segments and swapping their order. This procedure disrupts the temporal relationship between $\varphi_{low}(t)$ and $A_{high}(t)$ while preserving key characteristics such as their spectra. We then calculate the 99th percentile value, (k_{th}), which represents the CFC value greater than 99% of the samples across all surrogate data. All CFC values below k_{th} are set to zero. Subsequently, clusters of adjacent non-zero CFC values are identified within each dataset, both surrogate and non-surrogate. Each cluster is assigned a cluster score calculated as the sum of the values within the cluster. The CFC of the original data is considered significant at $p<0.01$ if its cluster score exceeds the 99th percentile of all surrogate cluster scores.

Cross Frequency Directionality

While the mean vector length metric effectively detects co-modulation of slow and fast components within a signal, it does not provide insights into potential temporal relationships between them. To address this limitation, we use the cross-frequency directionality (CFD) metric developed in [28]. CFD utilizes the phase slope index (PSI), which quantifies the directionality between two broadband signals, x and y, by analyzing the relationship of their phase difference,

$\Delta\varphi=\varphi_x-\varphi_y$ as a function of frequency. When the phase differences are linearly dependent on frequency, it indicates a fixed time lag between the two signals. Specifically, if $\Delta\varphi$ increases with frequency, x leads y; conversely, if $\Delta\varphi$ decreases, y leads x.

In more detail, the PSI is calculated as follows. First, we compute the Fourier Transform of the signals x and y denoted X and Y, respectively. These series are then split into N smaller segments and the complex coherence is computed:

$$C(f) = \frac{\sum_{i=1}^{N} X \cdot Y^*}{\sqrt{\sum_{i=1}^{N} |X|^2 \sum_{i=1}^{N} |Y|^2}}, (1)$$

where '*" denotes the complex conjugate. Then, the phase slope index is calculated as:

$$PSI(f_i) = Im(\sum_{f_i-\frac{\beta}{2}}^{f_i+\frac{\beta}{2}} C^*(f_j) C(f_j + \Delta f)), (2)$$

where "Im" refers to imaginary part. In cross-frequency analysis, the PSI is adapted by when y is not a signal independent from x, but rather the amplitude of x filtered around a high frequency, f_{high}. Finally, to emphasize the directionality of regions exhibiting strong cross-frequency coupling, we apply the masking technique described in [12]. Specifically, we normalise the CFC so that it takes values between 0 and 1, thus creating a mask. The final CFD is then calculated as the phase slope index multiplied by this mask.

To statistically assess the significance of the results, we employ the same procedure as for CFC for the highest 99th quantile. We also repeat the process for values lower than the 1st quantile in order to detect regions of significant negative CFD [28].

From spikes to continuous timeseries

As part of the analysis, we examined the instantaneous output of a population. To transform discrete spike events into continuous time series, we applied a decaying exponential kernel with a 5 ms time constant. This specific kernel was chosen to avoid introducing spiking information into the past, an issue associated with symmetric kernels like the Gaussian kernel or sliding window averages. Additionally, the decay time was selected to approximate the AMPA

receptor decay time, ensuring that the resulting output mimics the excitatory synaptic currents observed in downstream network layers.

Mutual Information

Mutual Information (MI) captures the dependence or shared information between two variables, providing insight into how much knowing one variable reduces uncertainty about the other. This metric is non-negative, with a value of zero indicating complete independence between the distributions of the two variables. The MI is calculated using the following expression:

$$MI = \int_X \int_Y p_{X,Y}(x,y) \log \frac{p_{X,Y}(x,y)}{p_X(x)p_Y(y)} dxdy, \quad (3)$$

where X(t) and Y(t) are continuous random variables, with probability distributions p_X and p_Y and joint probability distribution $p_{X,Y}$. Since the exact probability distributions are unknown and we only have a sample of them, estimating the distributions of Eq. 3 is not straightforward. To that matter, we utilized the "mutual_info_regression" function from [42] which employs a nearest-neighbor approach for the estimation of the probability densities function. In cases where we calculate MI between the input and output of networks, the analysis was repeated while temporally shifting the ouput to account for delays in the integration. For example, the observed differences in the delay at which MI peaks between the encoding of the θ input (Fig. 5c) and the parallel pathway (Fig. 5d) primarily reflect their distinct, explicitly set, transmission delays: 20 ms for θ and 0 ms for the parallel pathway.

Results

Cross-frequency coupling and directionality depend on connectivity

As an illustrative example and starting point for the present modeling work, we present electrophysiological recordings from the hippocampus of rats performing a contextual learning task. These data revealed strong CFC between the phase of theta and the amplitude of gamma oscillations recorded in pathway-specific field potentials, including the CA3 to CA1 connection (Schaeffer collateral, Sch), the entorhinal cortex layer III (ECIII) input to the CA1 region, and the layer II

(ECII) input to the Dentate Gyrus (Fig. 1a; data from [12]). Importantly, in all three cases, we experimentally demonstrated a gamma-to-theta interaction, revealed by negative coupling values in the CFD index (Fig. 1a-iii, 1a-v, and 1a-vii). Following previous studies, all CFD values presented here were renormalized to enhance regions of high CFC, with statistical significance ($p<0.01$) determined through surrogate analysis of clusters exhibiting the highest CFD absolute values [28,12]. For more details see also the analysis section.

To investigate theta-gamma interactions, we adapted the well-established circuit motifs Interneuron Network Gamma (ING) and Pyramidal-Interneuron Network Gamma (PING) [31, 33, 34, 35], with the addition of an external theta input (Fig. 1b-i and 1c-i). We began by analyzing separately the two circuit motifs, named as θ-ING and θ-PING respectively. Both models include a population of pyramidal cells (PCs) excited by a θ-modulated external input, with gamma rhythms generated locally by a population of fast-spiking self-inhibitory interneurons, the basket cells (BCs), which also project to the soma of the PCs. All connections and parameters for the two motifs were identical, except for the nature of the BC-PC connection: feedforward in θ-ING and feedback in θ-PING. For more details on the model see the methods section.

The distinct dynamics of these two circuit motifs are shown in Fig. 1b-ii and Fig. 1c-ii, where we visualise the raster plots for the PCs and BCs (blue and orange dots, respectively). In the same panels we superimposed the mean somatic membrane potential (V_{PC}) and the mean transmembrane somatic currents i_{transm}, across all PCs. Both motifs exhibited strong theta-gamma CFC (see Fig. 1b-ii,vi and 2b-ii,vi) but, importantly, opposite interaction directionality measured by CFD. In the θ-ING model (see Fig. 1b-v,vi), gamma activity anticipated the theta oscillation, resulting in a negative CFD in areas of high CFC. In the θ-PING model, each cycle begun with PC depolarization driven by the theta input, which, through the feedback connection, recruited BCs and induced gamma rhythmicity. As a result, theta activity preceded gamma, leading to a positive CFD (see Fig. 1c-v,vi).

We further explored the θ-ING results, which matched the experimental findings [12,29]. We first verified that negative CFD was not an artifact of higher theta harmonics or non-sinusoidal waveforms, which could generate spurious CFC and CFD values [43]. To address this, we systematically varied the transmission delay $\tau_{\theta,PC}$=10/20/30 ms between the theta input and the PCs while keeping the transmission delay between the theta input and the BCs constant at $\tau_{\theta,PC}$=20 ms. Thus we varied the relative transmission delay $\Delta\tau=\tau_{\theta,BC}-\tau_{\theta,PC}$ that controls the temporal relationship between gamma and theta (Fig. 2). For $\Delta\tau=-10$ ms, where the theta input reaches BCs earlier than the PC dendrites, gamma precedes theta activity more strongly, resulting in a more pronounced negative CFD (Fig. 2b, top panel). Conversely, for $\Delta\tau=10$ ms (Fig. 2b, bottom panel), gamma is relayed to PCs later than theta, causing CFD to switch to positive. For comparison and

completeness, $\Delta\tau$=0 ms, in which theta input reaches both populations simultaneously and results in negative CFD (Fig. 1b), was also included (Fig. 2b, middle panel). Overall, these results rule out a spurious contribution of theta harmonics or wave shape to the sign of CFD.

To explain why gamma-to-theta interaction is detected when no relative transmission delay between them exists, we examined the relationship between the externally imposed theta input and neuronal activity in both PC and BC populations (Fig. 2c and 2d). To that matter, we assigned to each PC and BC spike the theta phase associated to the synaptic current of the theta input in the distal dendrite of the PC (see Supplementary Fig. 1 for the same analysis using the external θ input as reference). When $\Delta\tau \leqslant 0$ ms, BC activity increases faster than the external input to the PCs (Fig. 2c). Consequently, feedforward gamma inhibition reaches the PC soma before the excitatory theta activity propagates from the distal dendritic compartment.

An important observation is that the timing of theta-nested gamma inhibition modulates the phase difference between the externally imposed theta and the locally generated theta oscillation (measured at the soma) (Fig. 2d). This mechanism may facilitate the coordination of theta rhythms across pathway-specific field potentials observed experimentally [12]. Furthermore, as evident from Fig. 2d, the fine-tuning of gamma-theta interactions may serve as a mechanism for phase encoding by defining the temporal windows within the theta cycle in which cell assembly formation is possible.

Synaptic determinants of gamma-to-theta interactions in the θ-ING model

To elucidate the synaptic mechanisms underlying gamma-to-theta interactions, we systematically increased synaptic strengths within the θ-ING model and evaluated their impact on CFC and neuronal theta firing patterns (Fig. 3). Notably, our findings indicate that CFD in the θ-ING model remains negative across a broad range of synaptic weights (see Table S3) and PC activity (see Table S4), with positive or negligible CFD values observed only at extreme parameter values.

We first examined the influence of synapses projecting to PCs. When inhibition is very high relative to excitation (Fig. 3a-iv and 3b-i) PCs spike only when the BCs' activity is at its lowest. Thus pyramidal spiking is scarce and out of phase with the external input, while the CFD is positive. Conversely, when excitatory input is excessively high relative to inhibition, PCs dominate the network dynamics, overriding BC-driven gamma oscillations (60–80 Hz), thereby disrupting CFC within this frequency band (Fig. 3a-i and 3b-iv). This effect is particularly pronounced when synaptic excitation surpasses the dendritic spiking threshold (Fig. 3b-iv). Under these conditions, the external theta generator, through dendritic spikes, regains control over network dynamics, with CFC shifting toward higher theta harmonics. In contrast,

when excitation and inhibition are balanced, PC spiking occurs slightly after the peak of synaptic input (Fig. 3b-v). Then, the temporal delay between input arrival and spiking, as well as the coupling strength between internal and external theta rhythms, is modulated by the level of the excitation/inhibition balance. Higher inhibitory input broadens the temporal distribution of spiking, thereby reducing the correlation between internal and external theta oscillations.

We next investigated the role of excitatory input to BCs (Fig. 3c). This synaptic connection not only regulates BC activity and, consequently, the total inhibitory drive to PCs but also modulates the frequency of the network's collective oscillations. Increased excitatory drive to BCs accelerates network dynamics, consistent with previous computational studies of ING models. Overall, our results demonstrated that θ-ING networks exhibit flexible dynamics, capable of modulating both single-cell and population-level activity through synaptic plasticity, while remaining in a mode where gamma leads theta locally.

Circuits of combined θ-ING and θ-PING motifs

Given that brain circuits are generally endowed with both feedforward and feedback inhibition simultaneously, we next investigated the dominant theta-gamma directionality in the combined model, by adding the feedback PC→BC connection to the θ-ING model or, equivalently, the feedforward θ→BC connection to the θ-PING model. Under these conditions, we found that mainly feedforward inhibition determined theta-gamma directionality, as shown by the positive to negative CFD transition when increasing the strength of the θ→BC connection, regardless of the strength of the PC→BC connection (Fig. 4a).

To understand better the differential role of these connections, we focused on the dynamics of the motifs that transition from a pure θ-PING to a mixed model of mainly negative directionality (Fig. 4b). By increasing the external θ excitatory drive to BCs, this input overcomes the excitation received from PCs through the feedback PC→BC connection. Consequently, BCs predominantly fire earlier relative to the theta phase, resulting in a dominant gamma-to-theta interaction (see blue rectangle in Fig. 4b). Simultaneously, the earlier firing of BCs inhibits PCs, and further diminishes the influence of the feedback connection (PC→BC). Therefore, a single unified model with both feedforward and feedback connections reproduces the experimentally observed theta-gamma interactions in various systems and suggests that the directionality of this interaction can be controlled via a local feedforward inhibitory connection. We also note that strengthening the feedforward pathway was associated with an increase in the frequency of the gamma band nested to theta, while the opposite effect was observed with an increase in feedback connection strength.

Functional differences of θ-ING and θ-PING motifs

To this point, our analysis has concentrated on the circuit-level determinants of directionality in theta-gamma interactions. In the following section, we explored whether different directionality modes, either pure θ-ING and θ-PING or two mixed motifs (Cases 2 and 3, Fig. 5), offer distinct computational capacities. Recognizing that, in more natural circuits, neurons typically receive inputs from multiple sources, we extended our analysis to include two external input pathways. The first input was the θ-driven signal directed to the distal dendrites of PCs, as in previous analyses. The second input, called here the parallel pathway, targeted the proximal dendritic segment, consisting of pulses distributed according to a Poisson process.

To evaluate the computational properties of each motif, we employed two protocols. The first protocol assessed the encoding capacity by calculating the mutual information (MI) between an external input and its corresponding PC firing output. The second protocol evaluated the robustness to variability as the MI between outputs generated in response to an input (either the θ or the parallel pathway) whose realisation is fixed between simulations while all other inputs realisations vary (see Fig. 5a and the methods section for details on the protocols).

We identified a complementary relationship between the motifs in encoding information from both pathways. First, all motifs effectively encoded information from the θ-input, which serves as the primary driver of the circuit (Fig. 5c). However, each motif also demonstrated the flexibility to encode information from the parallel pathway (Fig. 5d). Notably, this flexibility was enhanced in ING-shifted configurations, whereas θ-input encoding was favored in PING-shifted motif configurations. The disparity between motifs arises from a fundamental difference, evident in the membrane potential traces shown in Fig. 1b, and 1c. In the pure θ-PING case, PCs and BCs are strongly coupled via feedback connections, resulting in more pronounced gamma oscillations than in the θ-ING motif. This creates a robust theta-gamma scaffold for encoding, where opportunity windows for encoding are restricted to the peaks of the gamma cycles nested within each theta cycle. Inputs that are not synchronized with this rhythmic theta-gamma structure, such as the parallel pathway, more often fail to evoke a PC response. In contrast, in the θ-ING motif, gamma oscillations are primarily driven by BCs in a feedforward manner and, while still nested within the theta cycle, this gamma activity is more loosely anchored to PC firing, broadening the temporal windows for encoding. Consequently, strong perturbations falling within or outside the theta-gamma coding framework are able to overcome depolarization thresholds. To support this interpretation, we conducted simulations where the parallel pathway was replaced with a single perturbation. This allowed us to assign a gamma phase to each perturbation, revealing that the θ-PING motif was most responsive during the peak of the gamma

oscillation, whereas the θ-ING motif exhibited firing throughout the cycle (see Supplementary Fig. 2), confirming our hypothesis.

Finally, we assessed encoding consistency under conditions of variability. Information encoding of the θ-input in PING-shifted motifs (Fig. 5c) was accompanied by greater consistency (Fig. 5e). Similarly, encoding of the parallel pathway was not only greater in ING-shifted motifs (Fig. 5d) but also more robust to variability (Fig. 5f). Overall, the continuous transition observed between the two models, modulated by the balance between feedforward and feedback inhibition, suggests a mechanism for weighting or selecting communication channels with different temporal structures, which could be reflected in the CFD index.

Discussion

In this study, we have shown that the directionality of theta-gamma interactions depends on, and can be regulated by, the feedforward and feedback inhibition balance. In our motifs, theta is an external oscillation that impinges on the distal dendrites of PCs, while gamma is locally generated by a population of inhibitory neurons. Specifically, we found that circuit motifs with enhanced theta-modulated feedforward inhibition (θ-ING) exhibit dominant gamma-to-theta interactions, while those with enhanced theta-modulated feedback inhibition (θ-PING) display dominant theta-to-gamma interactions. In a combined circuit containing both feedforward and feedback connections, we found that the feedforward connection determines theta-gamma directionality and governs the transition between interaction modes.

We further found that these operational modes significantly influence the firing phase of PCs within the theta cycle. The feedback-feedforward inhibitory balance implements a push-pull mechanism that governs the firing phase of PCs: Increased feedforward inhibition leads to phase precession and increased feedback inhibition induces phase recession. Furthermore, we showed that these operational modes also modulate the responsiveness of PCs to inputs with different temporal structures. The constraints imposed by a particular theta-gamma coupling mode define specific opportunity windows during which PCs can fire. By fine-tuning the timing between slow and fast oscillations, this mechanism selectively prioritizes information transmitted through independent afferent pathways, enhancing computational flexibility. In the following sections, we explore the practical applications and limitations of our model and discuss its relevance to experimentally observed brain dynamics.

Is θ-ING a realistic model for negative CFD?

The emergence of negative cross-frequency directionality in the θ-ING model is critically dependent on the rapid response of BCs, enabling gamma oscillations to precede local theta rhythms. This raises an important question regarding the physiological validity of the conditions assumed in our model. We argue that our implementation of BC activation times is, in fact, conservative.

First, dendritic transmission in BCs is notably rapid, with evoked postsynaptic currents at distal dendritic sites depolarizing the soma within less than the 1 ms dendritic delay [39]. Second, stimulation of the Schaffer collateral induces monosynaptic excitation [44] followed by disynaptic inhibition after only 1.9 ± 0.2 ms delay. This is faster, on average, than the delays assumed in our model, which consist of the 1 ms dendritic delay plus 1.5 ± 0.2 ms of synaptic delay from BC to PCs and the spike generation time. Third, both *in vivo* and *in vitro* patch-clamp recordings from the CA1 region have demonstrated faster action potential initiation in BCs compared to PCs following stimulation of pathways that simultaneously excite BCs and PCs, namely the perforant path and the Schaffer collateral, respectively [45, 46]. Finally, regarding population dynamics, *in vivo* recordings from mice running in a maze, which are dominated by strong theta rhythmicity in the hippocampus, have shown that interneurons activity in the pyramidal layer of CA1 peaks approximately 60 degrees (or equivalently 20 ms) ahead of the theta phase of PCs (see Fig. 5 in [47]). This finding is consistent with our results (Fig. 2c and 2d), which show that BCs lead PCs significantly in theta phase. Taken together, these findings support the plausibility of the inhibitory time delays implemented in our model.

Limitations

Our model is intentionally minimal, designed to ensure the reported directionalities are broadly applicable across different brain regions, as supported by existing literature [28, 29, 48, 12, 50, 51]. This generalizability, however, comes at the expense of region-specific precision. While addressing such specificity would require detailed multicompartmental models tailored to particular brain areas [52, 53, 54], the simplicity of our model allows it to capture fundamental dynamics effectively. Future work incorporating diverse interneuron types and their unique connectivity patterns, particularly in regions like the hippocampus, would further refine our understanding [55].

While the motifs reproduces gamma-to-theta and theta-to-gamma directionalities, they do not account for large cross-frequency lags, such as the -50 ms lag observed in human auditory cortex electrocorticogram data [29]. However,

by accounting for plausible relative transmission delays, as illustrated in Fig. 2, the motifs can accommodate a wide range of experimentally observed cross-frequency lags. These lags may reflect multi-synaptic pathways. For instance, in the CA3 region, long-lag negative CFD could arise if BCs are monosynaptically recruited by entorhinal cortex inputs, while PCs are driven through the disynaptic circuit (EC→DG→CA3). Investigating these delays in specific anatomical contexts offers promising opportunities for future research.

We do not address different potential mechanisms of CFC generation. In our model, external theta rhythms drive local interneurons and PCs to generate local gamma and theta oscillations. This design aligns with patch-clamp recordings highlighting the role of local inhibition in gamma generation, as well as with LFP recordings between distant sites in the hippocampus that exhibit high coherence in the theta but not in the gamma band [26, 24, 56, 25]. However, in experiments recording theta-gamma CFC in connected layers of the hippocampal formation, it has been shown that the upstream theta-gamma activity may influence downstream CFC dynamics [21, 22, 23, 57]. These findings suggest that the generation of CFC may be contributed by both local and network mechanisms. Interestingly, in our model, the firing of the PCs, both in the θ-ING and θ-PING motifs, relays a theta-gamma coupled output to a potential downstream target (V_{PC} traces of Fig. 1). Therefore, although our primary focus has been on the directionality of cross frequency interactions, the model captures key insights into the generation of cross-frequency coupling (CFC) and provides a valuable framework for further exploration. How do local and network mechanisms of CFC generation interact and how the interaction conditions firing sequences and information transmission? Future work will address this question.

In summary, despite its simplifications, the model offers a robust framework for understanding CFC and CFD across regions while paving the way for more detailed, region-specific explorations in future studies.

Interpretation of CFD measurements

Our results suggested that the balance between feedforward and feedback inhibition in local circuits determines the directionality of cross-frequency interactions. We further showed that a feedback-shifted balance favours transmission in an afferent pathway by promoting the specific cross-frequency rhythmicity driven by the afferent input, while a feedforward-shifted motif broadens the opportunity window for encoding, facilitating parallel pathways to transmit. Accordingly, dynamic CFD measures could be interpreted in terms of predominant inhibitory circuit motifs and prioritization of functional connectivity pathways.

A recent study using electrocorticography in human epilepsy patients performing a spatial attention task reported a relationship between alpha-gamma CFD values and attentional states [51]. Specifically, more negative CFD values were associated with non-attended stimulus, while lower absolute (but still negative) CFD values were linked to attended stimulus. According to our model, less negative CFD would be reflecting a PING-shifted circuit state that favors transmission of the message in the afferent (attended) pathway, in this case, the visual dorsal stream, reducing the impact of parallel (distracting) inputs. Similarly, a more negative CFD, as found for non-attended stimulus, is expected from an ING-shifted circuit in which parallel inputs gain relevance over the afferent pathway. Importantly, the authors reported enhanced functional connectivity along the visual dorsal stream in the first case, and suppressed connectivity in the second, supporting our interpretation. The model offers a mechanism to explain attention deployment dynamically and flexibly, based on feedforward-feedback inhibitory balance and reflected in the CFD metric.

The previous study provides further experimental support to our model. First, alpha-phase activity in upstream regions preceded downstream high gamma activity, while locally, gamma preceded alpha [51], which aligns well with our model predictions (compare Fig. S1 with Fig. 2). Second, the model predicts an increase/decrease of the gamma frequency nested to the slow oscillation in ING/PING shifted circuits (Fig. 4), respectively. Experimentally, the peak of gamma nested to alpha decreased from 180-170 Hz to 150 Hz with attention, associated with a less negative CFD (Fig. 2 of [51]).

In the hippocampus, both positive and negative CFD values have been reported in different contexts [49, 29, 12]. For example, independent component analysis of local field potentials (LFPs) recorded from rats exploring various mazes identified gamma-to-theta interactions across three distinct synaptic pathways: CA3 to CA1, EC2 to DG, and EC3 to CA1 [12]. In contrast, LFP recordings from the pyramidal layer of CA1 in sleeping rats revealed positive CFD values [29]. According to our model, this discrepancy could reflect dynamic regulation of gamma-theta interactions across different behavioral states, such as active exploration vs. sleep, driven by distinct balances of feedforward and feedback inhibition. However, a note of caution is warranted regarding the use of independent components vs. raw LFPs. Since LFP signals reflect a composite contribution from multiple underlying synaptic pathways due to volume conduction effects [58], such effects could have influenced CFD measurements. Although a control analysis in [12] found negative CFD values also using LFPs, exhaustive comparative analysis was not performed. Future research in the hippocampus should include simultaneous recordings during different exploratory behaviors and sleep states within the same animals to directly test

the predictions of our model. Additionally, a quantitative analysis of CFD, rather than a qualitative assessment of positive versus negative values, would provide further validation of the proposed dynamic regulation of theta-gamma interactions.

In conclusion, we presented modeling results that propose a mechanism for the robust gamma-to-theta interactions observed in electrophysiological recordings, support the coexistence of both operational modes as a continuum rather than as conflicting options, and suggest a functional role in prioritizing parallel information pathways converging onto the same dendritic tree. A balance between feedforward and feedback inhibition lies at the core of this mechanism, and CFD or related measures may serve as valuable experimental entry points for understanding this process.

Competing interests

The authors have declared that no competing interests exist.

Author Contributions

Conceptualization: Dimitrios Chalkiadakis, Santiago Canals, Claudio R. Mirasso

Model development: Dimitrios Chalkiadakis, Jaime Sánchez-Claros

Analysis: Dimitrios Chalkiadakis, Santiago Canals, Victor J. López-Madrona

Preparation of the manuscript: Dimitrios Chalkiadakis, Santiago Canals, Claudio R. Mirasso, Jaime Sánchez-Claros, Victor J. López-Madrona

Acknowledgements

D. Chalkiadakis, J. Sanchéz- Claros and C. R. Mirasso acknowledge support from the Spanish Ministerio de Ciencia, Innovación y Universidades through projects PID2021-128158NB-C22 and María de Maeztu CEX2021-001164-M

funded by the MICIU/AEI/10.13039/501100011033. D. Chalkiadakis and S. Canals acknowledge support from the Spanish Ministerio de Ciencia, Innovación y Universidades through projects PID2021-128158NB-C21 and Severo Ochoa CEX2021-001165-S funded by the MICIU/AEI/10.13039/501100011033

We thank Spyridon Chavlis, Panayiota Poirazi and Oscar Herreras for their valuable comments.

Data availability statements

The electrophysiological datasets used in this study are available at: https://doi.org/10.20350/digitalCSIC/12537. Codes can be assessed at https://github.com/gerompampastrumf/thetaING_PING

References

1. Buzsáki G, Draguhn A. Neuronal Oscillations in Cortical Networks. Science. 2004 Jun;304(5679):1926-9.
2. Klimesch W. EEG Alpha and Theta Oscillations Reflect Cognitive and Memory Performance: A Review and Analysis. Brain Research Reviews. 1999 Apr;29(2-3):169-95.
3. Voytek B. Shifts in Gamma Phase–Amplitude Coupling Frequency from Theta to Alpha over Posterior Cortex during Visual Tasks. Frontiers in Human Neuroscience. 2010;4.
4. López-Madrona VJ, Canals S. Functional Interactions between Entorhinal Cortical Pathways Modulate Theta Activity in the Hippocampus. Biology. 2021 Jul;10(8):692.
5. Sławinska U, Kasicki S. The Frequency of Rat's Hippocampal Theta Rhythm Is Related to the Speed of Locomotion. Brain Research. 1998 Jun;796(1-2):327-31.
6. Wang XJ. Neurophysiological and Computational Principles of Cortical Rhythms in Cognition. Physiological Reviews. 2010 Jul;90(3):1195-268.
7. Fernández-Ruiz A, Sirota A, Lopes-dos-Santos V, Dupret D. Over and above Frequency: Gamma Oscillations as Units of Neural Circuit Operations. Neuron. 2023 Apr;111(7):936-53.
8. Douchamps V, Di Volo M, Torcini A, Battaglia D, Goutagny R. Gamma Oscillatory Complexity Conveys Behavioral Information in Hippocampal Networks. Nature Communications. 2024 Feb;15(1):1849.

9. Hyafil A, Giraud AL, Fontolan L, Gutkin B. Neural Cross-Frequency Coupling: Connecting Architectures, Mechanisms, and Functions. Trends in Neurosciences. 2015 Nov;38(11):725-40.
10. Tort ABL, Kramer MA, Thorn C, Gibson DJ, Kubota Y, Graybiel AM, et al. Dynamic Cross-Frequency Couplings of Local Field Potential Oscillations in Rat Striatum and Hippocampus during Performance of a T-maze Task. Proceedings of the National Academy of Sciences. 2008 Dec;105(51):20517-22.
11. Tort ABL, Komorowski RW, Manns JR, Kopell NJ, Eichenbaum H. Theta–Gamma Coupling Increases during the Learning of Item–Context Associations. Proceedings of the National Academy of Sciences. 2009 Dec;106(49):20942-7.
12. López-Madrona VJ, Pérez-Montoyo E, ´Alvarez-Salvado E, Moratal D, Herreras O, Pereda E, et al. Different Theta Frameworks Coexist in the Rat Hippocampus and Are Coordinated during Memory- Guided and Novelty Tasks. eLife. 2020 Jul;9:e57313.
13. Helfrich RF, Knight RT. Oscillatory Dynamics of Prefrontal Cognitive Control. Trends in Cognitive Sciences. 2016 Dec;20(12):916-30.
14. Fries P. Rhythms for Cognition: Communication through Coherence. Neuron. 2015 Oct;88(1):220-35.
15. Lisman JE, Jensen O. The Theta-Gamma Neural Code. Neuron. 2013 Mar;77(6):1002-16.
16. Rotstein HG, Pervouchine DD, Acker CD, Gillies MJ, White JA, Buhl EH, et al. Slow and Fast Inhibition and an H-Current Interact to Create a Theta Rhythm in a Model of CA1 Interneuron Network. Journal of Neurophysiology. 2005 Aug;94(2):1509-18.
17. Gloveli T, Dugladze T, Rotstein HG, Traub RD, Monyer H, Heinemann U, et al. Orthogonal Arrangement of Rhythm-Generating Microcircuits in the Hippocampus. Proceedings of the National Academy of Sciences. 2005 Sep;102(37):13295-300.
18. Orban G, Kiss T, ´Erdi P. Intrinsic and Synaptic Mechanisms Determining the Timing of Neuron Population Activity During Hippocampal Theta Oscillation. Journal of Neurophysiology. 2006 Dec;96(6):2889-904.
19. Tort ABL, Rotstein HG, Dugladze T, Gloveli T, Kopell NJ. On the Formation of Gamma-Coherent Cell Assemblies by Oriens Lacunosum-Moleculare Interneurons in the Hippocampus. Proceedings of the National Academy of Sciences. 2007 Aug;104(33):13490-5.
20. Stark E, Eichler R, Roux L, Fujisawa S, Rotstein HG, Buzsáki G. Inhibition-Induced Theta Resonance in Cortical Circuits. Neuron. 2013 Dec;80(5):1263-76.

21. Schomburg EW, Fernández-Ruiz A, Mizuseki K, Ber ´enyi A, Anastassiou CA, Koch C, et al. Theta Phase Segregation of Input-Specific Gamma Patterns in Entorhinal-Hippocampal Networks. Neuron. 2014 Oct;84(2):470-85.
22. Fernández-Ruiz A, Oliva A, Nagy GA, Maurer AP, Ber ´enyi A, Buzsáki G. Entorhinal-CA3 Dual-Input Control of Spike Timing in the Hippocampus by Theta-Gamma Coupling. Neuron. 2017 Mar;93(5):1213-26.e5.
23. Fernández-Ruiz A, Oliva A, Soula M, Rocha-Almeida F, Nagy GA, Martin-Vazquez G, et al. Gamma Rhythm Communication between Entorhinal Cortex and Dentate Gyrus Neuronal Assemblies. Science. 2021 Apr;372(6537):eabf3119.
24. Pernía-Andrade AJ, Jonas P. Theta-Gamma-Modulated Synaptic Currents in Hippocampal Granule Cells In Vivo Define a Mechanism for Network Oscillations. Neuron. 2014 Jan;81(1):140-52.
25. Zhou Y, Sheremet A, Kennedy JP, Qin Y, DiCola NM, Lovett SD, et al. Theta Dominates Cross-Frequency Coupling in Hippocampal-Medial Entorhinal Circuit during Awake-Behavior in Rats. iScience. 2022 Nov;25(11):105457.
26. Lasztoczi B, Klausberger T. Layer-Specific GABAergic Control of Distinct Gamma Oscillations in the CA1 Hippocampus. Neuron. 2014 Mar;81(5):1126-39.
27. Lakatos P, Shah AS, Knuth KH, Ulbert I, Karmos G, Schroeder CE. An Oscillatory Hierarchy Controlling Neuronal Excitability and Stimulus Processing in the Auditory Cortex. Journal of Neurophysiology. 2005 Sep;94(3):1904-11.
28. Jiang H, Bahramisharif A, Van Gerven MAJ, Jensen O. Measuring Directionality between Neuronal Oscillations of Different Frequencies. NeuroImage. 2015 Sep;118:359-67.
29. Dupré La Tour T, Tallot L, Grabot L, Doyere V, Van Wassenhove V, Grenier Y, et al. Non-Linear Auto-Regressive Models for Cross-Frequency Coupling in Neural Time Series. PLOS Computational Biology. 2017 Dec;13(12):e1005893.
30. Neymotin SA, Lazarewicz MT, Sherif M, Contreras D, Finkel LH, Lytton WW. Ketamine Disrupts Theta Modulation of Gamma in a Computer Model of Hippocampus. The Journal of Neuroscience. 2011 Aug;31(32):11733-43.
31. Wang XJ, Buzsáki G. Gamma Oscillation by Synaptic Inhibition in a Hippocampal Interneuronal Network Model. The Journal of Neuroscience. 1996 Oct;16(20):6402-13.

32. White JA, Banks MI, Pearce RA, Kopell NJ. Networks of Interneurons with Fast and Slow γ-Aminobutyric Acid Type A (GABAA) Kinetics Provide Substrate for Mixed Gamma-Theta Rhythm. Proceedings of the National Academy of Sciences. 2000 Jul;97(14):8128-33.
33. Börgers C, Kopell N. Synchronization in Networks of Excitatory and Inhibitory Neurons with Sparse, Random Connectivity. Neural Computation. 2003 Mar;15(3):509-38.
34. Börgers C, Kopell N. Effects of Noisy Drive on Rhythms in Networks of Excitatory and Inhibitory Neurons. Neural Computation. 2005 Mar;17(3):557-608.
35. Buzsáki G, Wang XJ. Mechanisms of Gamma Oscillations. Annual Review of Neuroscience. 2012 Jul;35(1):203-25.
36. Börgers C. An Introduction to Modeling Neuronal Dynamics. vol. 66 of Texts in Applied Mathematics. Cham: Springer International Publishing; 2017.
37. Sánchez-Claros J. Neural Dynamics and Information Transmission: From Cortical Circuits to the Hippocampal Modelling [Ph. D. thesis]. Palma de Mallorca: University of the Balearic Islands; 2024.
38. Parasuram H, Nair B, D'Angelo E, Hines M, Naldi G, Diwakar S. Computational Modeling of Single Neuron Extracellular Electric Potentials and Network Local Field Potentials Using LFPsim. Frontiers in Computational Neuroscience. 2016 Jun;10.
39. Hu H, Martina M, Jonas P. Dendritic Mechanisms Underlying Rapid Synaptic Activation of Fast-Spiking Hippocampal Interneurons. Science. 2010 Jan;327(5961):52-8.
40. Hines ML, Carnevale NT. The NEURON Simulation Environment. Neural Computation. 1997 08;9(6):1179-209.
41. Canolty RT, Edwards E, Dalal SS, Soltani M, Nagarajan SS, Kirsch HE, et al. High Gamma Power Is Phase-Locked to Theta Oscillations in Human Neocortex. Science. 2006 Sep;313(5793):1626-8.
42. Pedregosa F, Varoquaux G, Gramfort A, Michel V, Thirion B, Grisel O, et al. Scikit-learn: Machine Learning in Python. Journal of Machine Learning Research. 2011;12:2825-30.
43. Lozano-Soldevilla D, Ter Huurne N, Oostenveld R. Neuronal Oscillations with Non-sinusoidal Morphology Produce Spurious Phase-to-Amplitude Coupling and Directionality. Frontiers in Computational Neuroscience. 2016 Aug;10.
44. Pouille F, Scanziani M. Enforcement of Temporal Fidelity in Pyramidal Cells by Somatic Feed-Forward Inhibition. Science. 2001 Aug;293(5532):1159-63.

45. Sik A, Penttonen M, Ylinen A, Buzsaki G. Hippocampal CA1 Interneurons: An in Vivo Intracellular Labeling Study. The Journal of Neuroscience. 1995 Oct;15(10):6651-65.
46. Pouille F, Marin-Burgin A, Adesnik H, Atallah BV, Scanziani M. Input Normalization by Global Feedforward Inhibition Expands Cortical Dynamic Range. Nature Neuroscience. 2009 Dec;12(12):1577-85.
47. Csicsvari J, Hirase H, Czurkó A, Mamiya A, Buzsáki G. Oscillatory Coupling of Hippocampal Pyramidal Cells and Interneurons in the Behaving Rat. The Journal of Neuroscience. 1999 Jan;19(1):274-87.
48. Zheng J, Anderson KL, Leal SL, Shestyuk A, Gulsen G, Mnatsakanyan L, et al. Amygdala-Hippocampal Dynamics during Salient Information Processing. Nature Communications. 2017 Feb;8(1):14413.
49. Johnson EL, Adams JN, Solbakk AK, Endestad T, Larsson PG, Ivanovic J, et al. Dynamic Frontotemporal Systems Process Space and Time in Working Memory. PLOS Biology. 2018 Mar;16(3):e2004274.
50. Jiang H, Bahramisharif A, Van Gerven MAJ, Jensen O. Distinct Directional Couplings between Slow and Fast Gamma Power to the Phase of Theta Oscillations in the Rat Hippocampus. European Journal of Neuroscience. 2020 May;51(10):2070-81.
51. Yang X, Fiebelkorn IC, Jensen O, Knight RT, Kastner S. Differential Neural Mechanisms Underlie Cortical Gating of Visual Spatial Attention Mediated by Alpha-Band Oscillations. Proceedings of the National Academy of Sciences. 2024 Nov;121(45):e2313304121.
52. Bezaire MJ, Raikov I, Burk K, Vyas D, Soltesz I. Interneuronal Mechanisms of Hippocampal Theta Oscillations in a Full-Scale Model of the Rodent CA1 Circuit. eLife. 2016 Dec;5:e18566.
53. Tzilivaki A, Kastellakis G, Poirazi P. Challenging the Point Neuron Dogma: FS Basket Cells as 2-Stage Nonlinear Integrators. Nature Communications. 2019 Aug;10(1):3664.
54. Bilash OM, Chavlis S, Johnson CD, Poirazi P, Basu J. Lateral Entorhinal Cortex Inputs Modulate Hippocampal Dendritic Excitability by Recruiting a Local Disinhibitory Microcircuit. Cell Reports. 2023 Jan;42(1):111962.
55. Tzilivaki A, Tukker JJ, Maier N, Poirazi P, Sammons RP, Schmitz D. Hippocampal GABAergic Interneurons and Memory. Neuron. 2023 Jul:S0896627323004750.
56. Gan J,Weng Sm, Pern´ıa-Andrade AJ, Csicsvari J, Jonas P. Phase-Locked Inhibition, but Not Excitation, Underlies Hippocampal Ripple Oscillations in Awake Mice In Vivo. Neuron. 2017 Jan;93(2):308-14.
57. Zutshi I, Valero M, Fern´andez-Ruiz A, Buzs´aki G. Extrinsic Control and Intrinsic Computation in the Hippocampal CA1 Circuit. Neuron. 2022 Feb;110(4):658-73.e5.

58. Herreras O, Makarova J, Makarov VA. New Uses of LFPs: Pathway-specific Threads Obtained through Spatial Discrimination. Neuroscience. 2015 Dec;310:486-503.

Figures

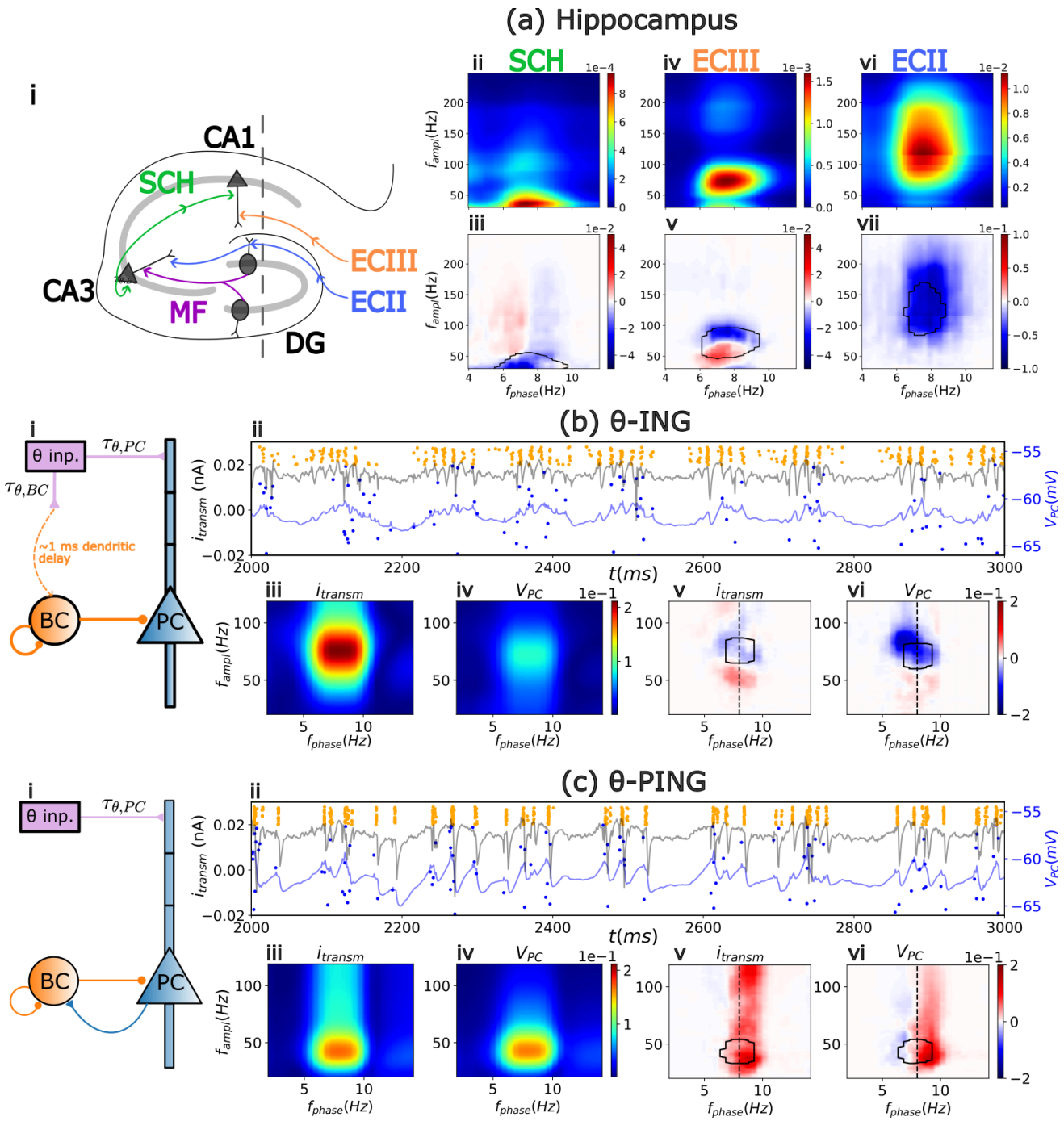

Fig. 1. Experimental and computational cross frequency coupling and directionality. (a) Cross-Frequency Coupling (CFC) and Cross-Frequency Directionality (CFD) in electrophysiological recordings from the rat hippocampus (data from [12]). Schematic representation of the hippocampus with the pathway-specific layers illustrated (i). Sch: Schaffer Collateral, MF: Mossy Fibers, ECII and ECIII: Entorhinal Cortex layers II and III, DG: Dentate Gyrus, CA1 and CA3: Cornu Ammonis. Theta-gamma CFC in the three layer-specific field potentials (a-ii,-iv,-vi) and their corresponding CFD (a-iii,-v,-vii). Note that all pathways exhibit on average CFD<0 for high CFC (black contour in CFD panels). (b) Circuit motif of the θ-ING model (i), with the resultant activity time courses (i_{transm}: average PC somatic transmembrane current; V_{PC}: average somatic PC membrane voltage) and raster plots of the BCs (orange dots) and PCs (blue dots) firing (ii). The corresponding CFC and CFD for the i_{transm} and V_{PC} are depicted in panels (iii and v) and (iv and vi), respectively. The black contour in CFD plots shows the 95 percentile of the respective CFC. (c) Same as (b) but for the θ-PING motif.

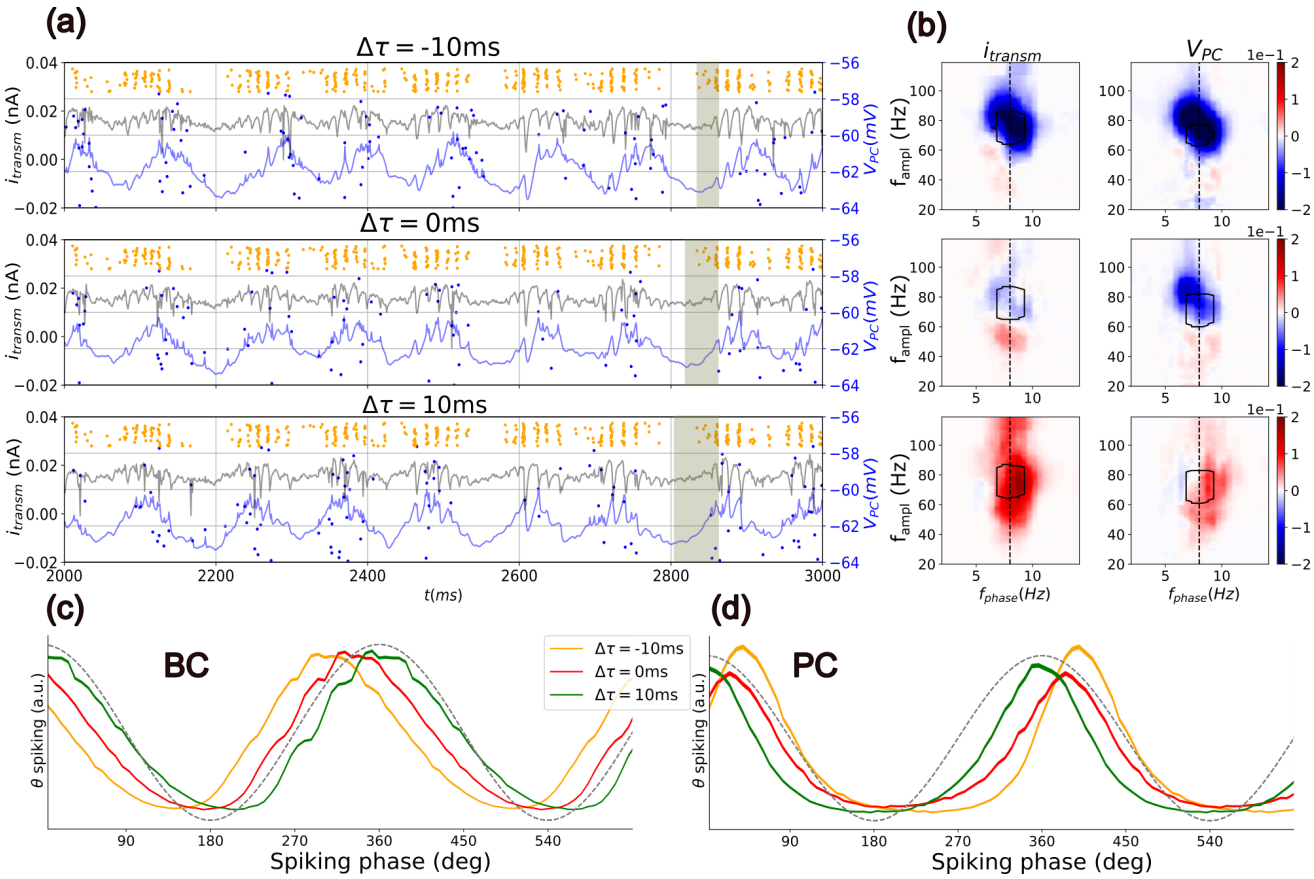

Fig. 2. Directionality in the θ-ING model reverses depending on the relative transmission delay. (a) Activity time courses and raster plots of the BCs (orange dots) and PCs (blue dots) firing, for the different relative transmission delay

Δτ. The shaded area highlights the relative displacement of the theta trough (minima of i_{transm}) with respect to the initiation of the gamma oscillation. (b) CFDs for i_{transm} and V_{PC}. Contour lines indicate the range of higher CFC (more than 95th percentile). Relative transmission delay Δτ=-10/0/10 ms increases from top to bottom in (a) and (b). (c-d) Theta-phase spiking profiles for BCs and PCs, respectively. Each spike is associated with the theta phase of the synaptic current measured at the distal dendrites of PCs (indicated by the dashed black line).

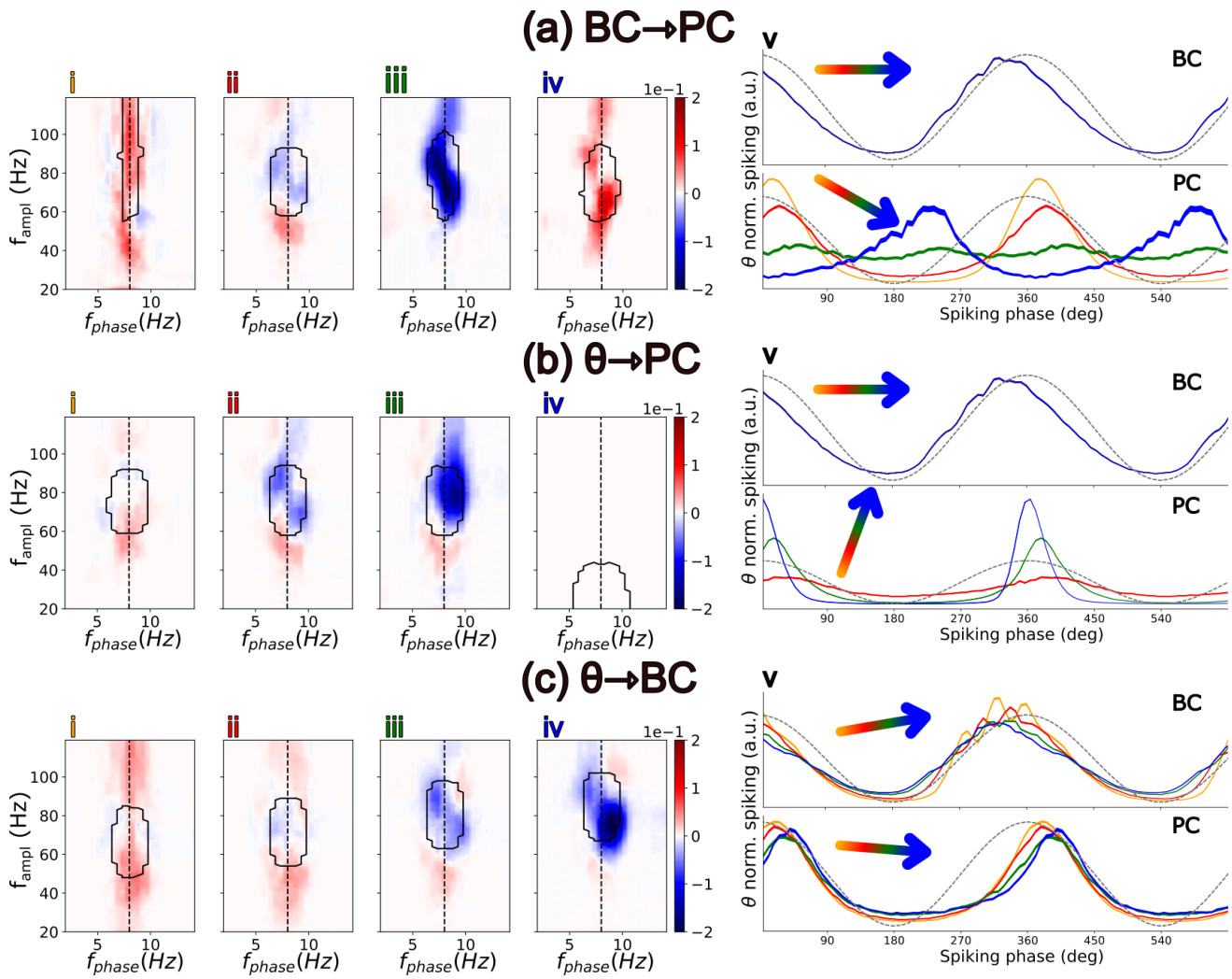

Fig. 3. Role of different synaptic coupling strengths on the θ-ING directionality, firing rate, and spiking phase. The synaptic coupling assumes four increasing values: $w_i<w_{ii}<w_{iii}<w_{iv}$ (see Table S3 for exact values) for the following connections: BC→PC (a), θ→PC (b), and θ→BC (c). (i-iv) CFD with the contour encircling areas of high CFC values. (v) Theta spiking profiles of the BC (Top) and PC (Bottom). Spikes are binned according to the phase of the synaptic current of the θ input in the PCs dendrites (same as in Fig. 2). Spiking distributions are normalized so that the integral

over a theta cycle is 1. The orientation of the coloured arrow indicates whether the firing rate increases, decreases, or remains the same as the corresponding synaptic weight increases (see Table S4 for exact values).

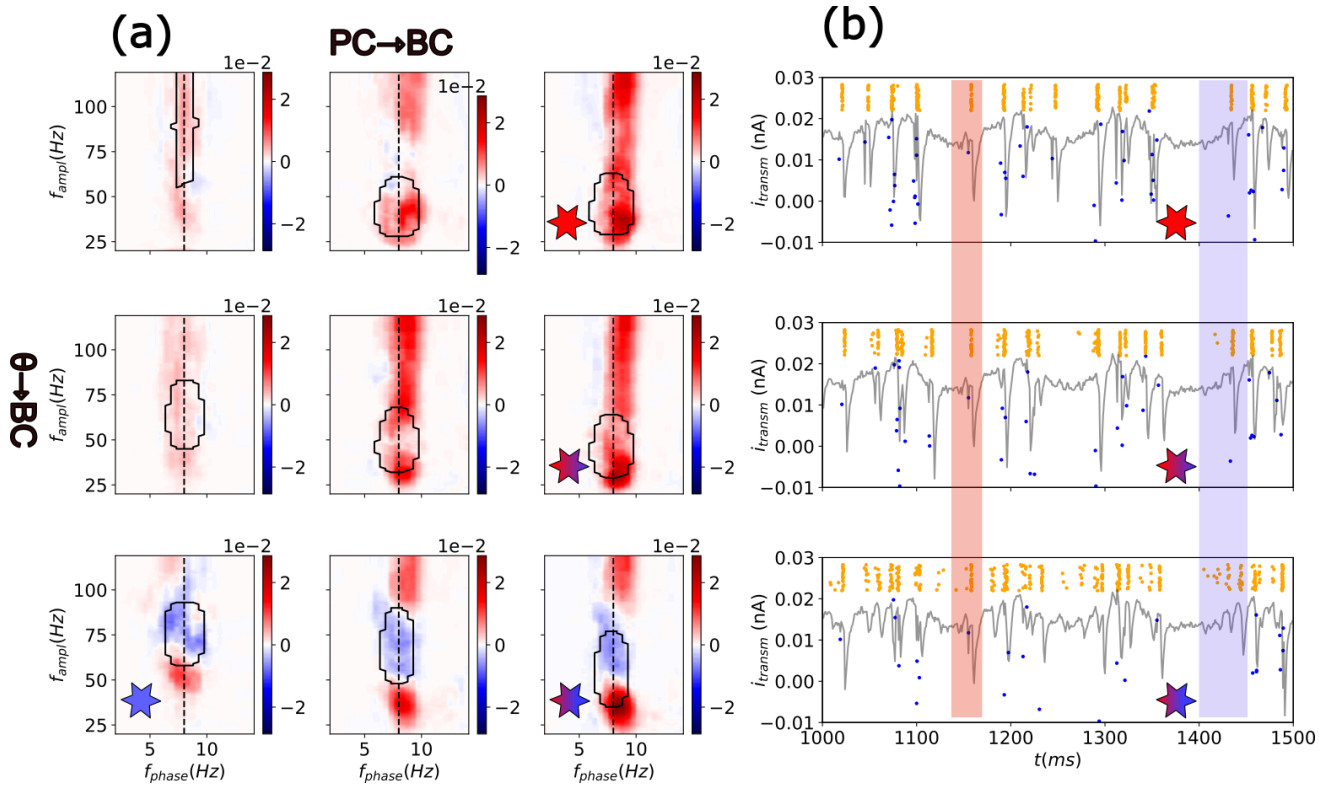

Fig. 4. Transitions between positive and negative CFD in a combined θ-ING and θ-PING circuit. (a) CFD in the 2D parameter space of the relevant synaptic weights PC→BC and θ→BC. The θ→BC input strength increases in rows from top to bottom. The PC→BC input strength increases in columns from left to right. Red and blue stars denote cases of pure θ-PING and θ-ING motifs, respectively (same motifs shown in Fig. 1). Stars of mixed colors depict a transition from a pure θ-PING to a mixed motif of predominantly opposite directionality. (b) Transmembrane currents and raster plots of this transition (same stars code as in panel a). Coloured rectangles highlight the initial part of a θ oscillation as well as the first few gamma cycles. The rectangles in blue depict an example of a theta cycle whose directionality transition from top (CFD>0) to bottom (CFD<0). Note how increasing feedforward inhibition advances the firing of BCs (orange dots in the raster plot), and consequently the gamma oscillations, over the theta cycle and the firing of PCs (blue dots). The rectangle in red depicts one example of theta cycle in which transition was not fully realized, highlighting the dynamic character of the CFD.

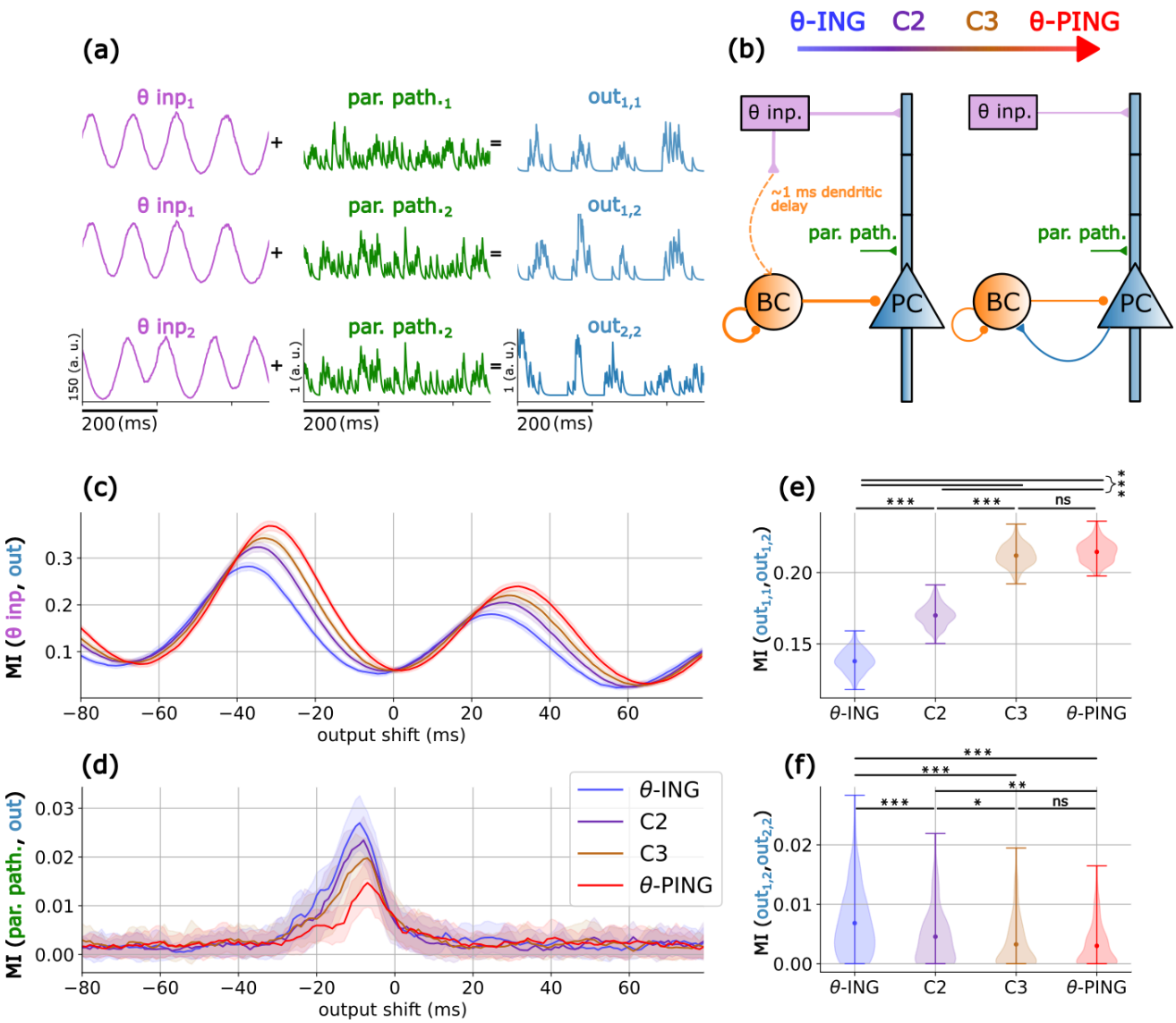

Fig. 5. Functional analysis of motifs with increasing CFD. (a) Schematic representation of the inputs in the θ (purple) and parallel (green) pathways and the outputs produced by the PCs of the models. All time series were generated by convoluting the spike trains with a 5 ms exponential decay kernel, thus their scale is in arbitrary units. (b) The θ-ING and θ-PING motifs with the parallel pathway introduced at a proximal dendritic segment of PCs. Cases 2 and 3 (C2 and C3, respectively) are the mixed motifs lying in intermediate values of the θ-ING and θ-PING parameter space. (c) Encoding computed as the Mutual Information (MI) between the θ input and the pyramidal output. Pairwise T-tests with Bonferonni correction for multiple comparisons between the peak MI values showed that all cases are significantly different ($p<0.001$). (d) Same as in (c) but considering the parallel pathway as input. All cases are significantly different ($p<0.001$) except for C3–θ-PING ($p<0.1$), and θ-ING–C2 and C2–C3 that are not sgnificantly different). (e) Consistency measured as MI between pairs of outputs in response to a constant θ input. (f) Same as in (e) but considering a constant parallel

pathway input instead. Stars in panels (e) and (f) depict significant differences using pairwise T-tests with Bonferonni correction: ***/**/* p<0.001/0.01/0.05, respectively.

Supporting Information

Table S1. Synaptic parameters of the model.

Receptor	τ_r(ms)	τ_d(ms)
AMPA	0.05	5.3
NMDA	15	150
GABA	0.07	9.1

Table S2. Synaptic weights for Fig. 1. The synaptic weight depicted for PC→BC is for the θ-PING, otherwise, it is zero. The synaptic weight depicted for θ-ING is for the θ→BC, otherwise, it is zero.

Connection	Post. Site	Receptor	g(μS)	#pres.
θ→PC	Distal	AMPA	0.04	500
		NMDA	0.004	500
BC→PC	soma	GABA	0.144	30
Noise→PC	soma	AMPA	0.22	1
Noise→PC	soma	GABA	0.24	1

Pois.→PC	Proximal	AMPA	0.01	1
		NMDA	0.001	1
BC→BC	soma	GABA	8.1	30
Noise→BC	soma	AMPA	0.08	1
Noise→BC	soma	GABA	2	1
PC→BC	soma	AMPA	40	80
		NMDA	4	80
θ→BC	soma	AMPA	0.5	500
		NMDA	0.05	500

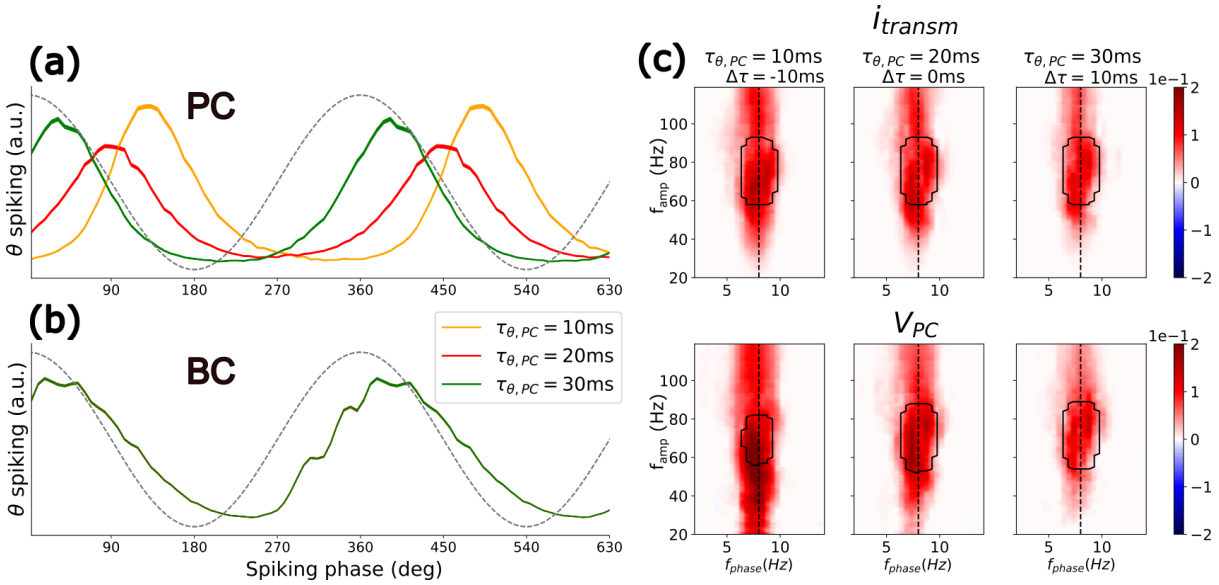

S1 Fig. Similar to Fig. 2, but using the external θ drive phase as the θ reference for spiking and CFD calculations. Panels (a) and (b) show the θ phase of PC and BC spiking, respectively. Panel (c) illustrates the CFD for i_{transm} (top) and V_{PC}

(bottom). To derive the θ phase of the external population, spikes are passed through a decaying exponential kernel with a 5 ms time constant. Note that when using the external population's θ phase, the BC phase remains unchanged, while the PC phase shifts significantly due to different offsets. Finally, as the local γ is consistently generated by the external θ driver, the CFD remains positive under all conditions.

Table S3. Total synaptic weights for Fig. 3 represented as the product of the synaptic weight and the number of presynaptic neurons.

Conn.	w_i	w_{ii}	w_{iii}	w_{iv}
BC→PC	0	$4.32 * 10^{-3}$ nS	$8.64 * 10^{-3}$ nS	$12.96 * 10^{-3}$ nS
θ→PC	0	$1.5 * 10^{-2}$ nS	$2.5 * 10^{-2}$ nS	$3.0 * 10^{-2}$ nS
θ→BC	$1.5 * 10^{-1}$ nS	$2 * 10^{-1}$ nS	$3 * 10^{-1}$ nS	$3.5 * 10^{-1}$ nS

Table S4. Mean firing rates for BCs ($f_{r,BC}$(Hz)) and PCs ($f_{r,PC}$(Hz)) in the θ-ING model for different synaptic weights **v=**($w_i<w_{ii}<w_{iii}<w_{iv}$) in the circuit connection (Conn.). The simulations are the same as in Fig. 3. Blue-colored cells depict motifs that exhibit negative CFD.

	$f_{r,BC}$(Hz)				$f_{r,PC}$(Hz)			
Conn.	w_i	w_{ii}	w_{iii}	w_{iv}	w_i	w_{ii}	w_{iii}	w_{iv}
BC→PC	11.81	11.81	11.81	11.81	1.85	0.48	0.13	0.06

θ→PC	11.81	11.81	11.81	11.81	0	0.22	1.31	6.39
θ→BC	5.62	8.71	14.71	17.18	0.95	0.67	0.34	0.27

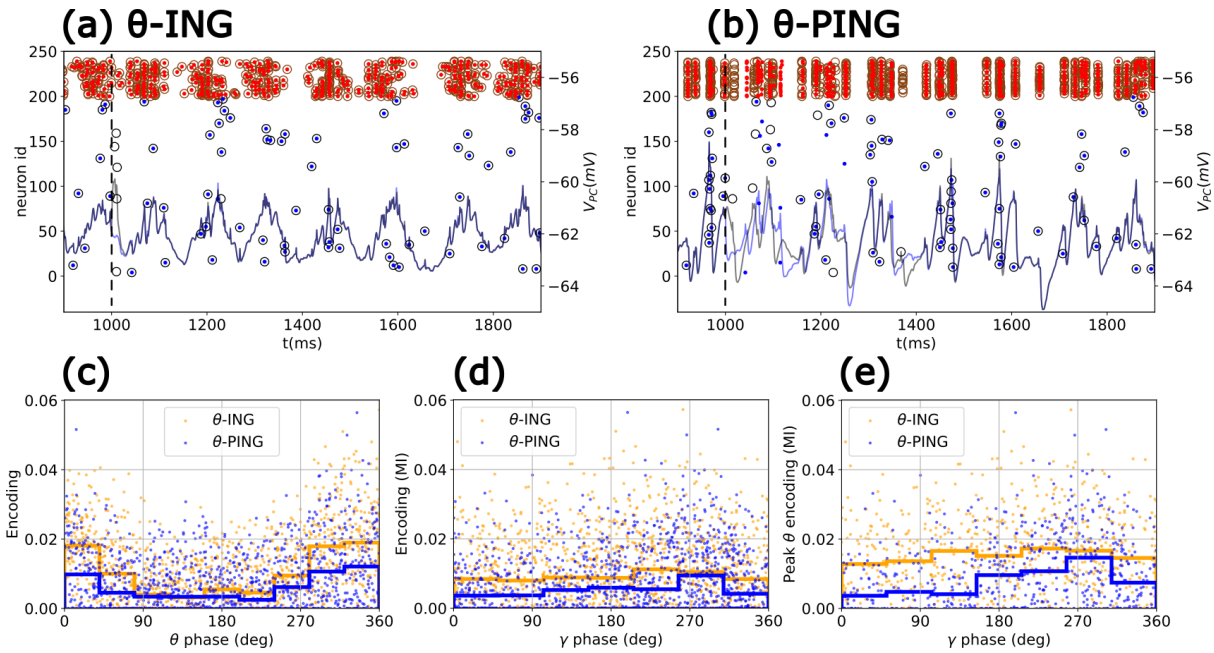

S2 Fig. Single perturbation analysis. A single spike is introduced in the proximal dendrite at a predefined time within the interval (1-1.5) s (specifically at 1 s, indicated by the black dashed line). Panels (a) and (b) show the dynamics for a θ-ING and a θ-PING motif, respectively, both with similar firing rates. Blue lines represent the mean membrane potential at the PC soma ($V_{PC,g}$) for the unperturbed case, while gray lines show the evolution after the perturbation ($V_{PC,p}$). Open circles indicate spikes in the perturbed simulations (gray for PCs, brown for BCs), and solid circles represent spikes in the baseline condition (blue for PCs, red for BCs). Since only one perturbation is applied, the resulting encoding value between output and perturbation can be related to the network state at the time of perturbation. (c) Encoding values are plotted against the θ phase of $V_{PC,p}$, where 180° represents the trough and 0°/360° the peak. (d) Same as (c), using a high-pass filter cutting of frequencies lower than 20Hz to capture the gamma activity of both motifs. (e) Same as (d), but for encoding values only when the θ phase is between -90° and 90°, i.e., when the network is more depolarized.